Available online at www.sciencedirect.com
ScienceDirect
Trans. Nonferrous Met. Soc. China 34(2024) 3992−4004
Transactions of Nonferrous Metals Society of China
www.tnmsc.cn

Additive manufacturing of pure copper via vat photopolymerization with slurry

An-liang YE[1], Meng WANG[1], Yan-bin JIANG[1], Xiao-zan WU[1], Chao-qun PENG[1], Jin HE[2], Xiao-feng WANG[1,3]

1. School of Materials Science and Engineering, Central South University, Changsha 410083, China;
2. Key Laboratory of Materials for High Power Lasers, Shanghai Institute of Optics and Fine Mechanics, Chinese Academy of Sciences, Shanghai 201800, China;
3. State Key Laboratory of Powder Metallurgy, Central South University, Changsha 410083, China

Received 30 June 2024; accepted 19 November 2024

Abstract: Stereolithography (SLA) combined with a two-step post-processing method "oxidation−reduction" was developed to fabricate pure copper with high complexity. The copper slurries for SLA were prepared, and particularly the influence of volume fraction of copper on the properties of copper slurries was investigated. In the two-step post-treatment process, organics were removed by oxidation and copper powder was oxidized simultaneously, and then the oxidized copper was reduced into highly reactive copper particles, improving the sintering activity of the copper green body and enhancing the relative density of the sintered part. The results show that curing depth of the copper slurries decreased with the increase of volume fraction of copper. The viscosity of the pure copper slurry rises exponentially as the volume fraction of copper exceeded 50%. The highest volume fraction of pure copper slurry for SLA is 55%. The specimens exhibited an increase in hardness and electrical conductivity with the increase of volume fraction of copper. Specifically, the maximum values of hardness and conductivity of samples with 55 vol.% copper were HV 52.7 and 57.1%(IACS), respectively.

Key words: pure copper; additive manufacturing; stereolithography; complex structure parts; copper slurry

1 Introduction

Pure copper exhibits high electrical conductivity, thermal conductivity, ductility, corrosion resistance, and antibacterial catalytic effect, making it widely utilized in electronics, aerospace, transportation, and medical treatment [1−5]. In recent years, with the aerospace and electronics industries rapidly evolving towards miniaturization and high integration, pure copper has to meet the requirements of high precision and complexity. Conventional pure copper manufacturing technologies, including casting, forging, extrusion, and powder metallurgy (PM), are hardly able to fabricate high-complexity parts [6−9]. Moreover, these technologies suffer from the defects of high cost, laborious manufacturing processes, low precision, and lengthy manufacturing cycle time [10]. Consequently, new technologies that address the above issues are desperately needed to keep up with the advancements in the electronics and aerospace fields.

Additive manufacturing, which offers integrated shaping, material savings, and high efficiency [11−14], has been employed to create highly complex and porous pure copper parts to address the ever-increasing criteria for heat dissipation. Up to now, most studies in the field of additive manufacturing technologies for pure copper have predominantly centered around the direct additive manufacturing

Corresponding author: Xiao-feng WANG, Tel: +86-13467516329, E-mail: 13467516329@163.com
DOI: 10.1016/S1003-6326(24)66653-7

technologies (DAMT) such as laser powder bed fusion (L-PBF) [11,15], and electron beam powder bed fusion (EB-PBF) [16,17]. However, it is difficult to fabricate pure copper parts by DAMT because of the high laser reflectivity and high thermal conductivity of copper powder, resulting in the drawbacks of high energy consumption, unstable melt pool, and high residual stress in copper parts [15,17,18]. As a result, DAMT is challenging to be used for pure copper, which is not consistent with alumina and titanium alloys [19,20]. SILBERNAGEL et al [21] utilized a small laser power of 200 W to fabricate pure copper parts, and the density and electrical conductivity of final part densities were only 85.6% and 50.3%(IACS), respectively, due to the high reflectivity properties of copper to near-infrared lasers resulting in insufficient laser energy deposited on the powder. COLOPI et al [22] employed a 1 kW single-peak laser to produce pure copper, yielding a final component with relative density more than 97%, but introducing large thermal stresses within the part and significant anisotropy in performance. In addition, the high reflectivity of copper poses a constant risk of damaging laser optics, giving rise to high maintenance and operating costs [23]. DAMT relying on arcs and electron beams, such as EB-PBF, avoids the concern about the energy absorption rate of copper powders, but inevitably introduces high equipment costs, large stress residues, and performance anisotropy [16].

Fortunately, indirect additive manufacturing technology such as binder jet printing (BJP) and vat photopolymerization (VPP) could prevent the aforementioned problems [18,24]. In particular, VPP mainly encompassing stereolithography (SLA) and digital light processing (DLP), even owns advantages including high strength of the green bodies, micron-level precision, and excellent surface quality [25]. Nevertheless, owing to the settlement of copper slurry, the tendency of copper powder to agglomerate, and the large difference in refractive index between copper powder and resin, there are only few reports on manufacturing pure copper parts via VPP [26,27]. JAVED et al [26] utilized VPP to prepare copper components and optimized the viscosity of the copper slurry, but the maximum relative density of samples was only 57%. In the recent work of LI et al [27], precursors (copper salts and copper oxide particles) were mixed with photosensitive resin to prepare slurry, and then DLP technology was employed in combination with reducing atmosphere sintering to successfully prepare copper foam, but the copper foam has low densities, resulting in limited application scenarios.

In this work, complex and relatively dense pure copper parts were fabricated by SLA combined with a two-step post-treatment route. The impact of dispersant type and content on slurry viscosity was systematically investigated. The effects of copper volume fraction on the viscosity and light curing ability of slurries were studied. In particular, a two-step post-treatment route, debinding in oxidation first and sintering in reduction atmosphere subsequently, was proposed to reduce the residual carbon rate and enhance the sintering activity of samples. Copper parts fabricated by SLA were characterized in terms of relative density, dimensional shrinkage, morphology, and specimen properties. This work is highly significant for SLA in the fabrication of pure copper and other metals.

2 Experimental

2.1 Materials

A micro-sized copper powder (Ruiying Technology Co., Ltd., China) was used as the raw material. Photosensitive monomers included 1,6-hexanediol diacrylate (HDDA, SARTOMER Chemicals Ltd.) and trimethylolpropane triacrylate (TMPTA, SARTOMER Chemicals Ltd.). ZN-1344 was used as the dispersant, and 2,4,6-trimethylbenzoyl diphenylphosphine oxide (TPO, KING CHEMICAL, Shanghai, China) served as photo initiator.

Scanning electron microscopy (SEM, Phenom XPro, Holland) was used to observe the particle morphology of the copper powder, and laser particle sizer (BT−9300ST, Dandong Baite Instrument Co., Ltd., China) was used to measure the particle size distribution which was determined by gauging the intensity and angle of the scattered light. Figure 1 displays SEM image and the particle size distribution of copper powder; its particle size D_{50} was 14.4 μm.

2.2 Preparation of copper slurry

Firstly, TMPTA and HDDA were added to a beaker at a mass ratio of 7:3 and stirred by a magnetic stirrer for 30 min to obtain the photosensitive resin

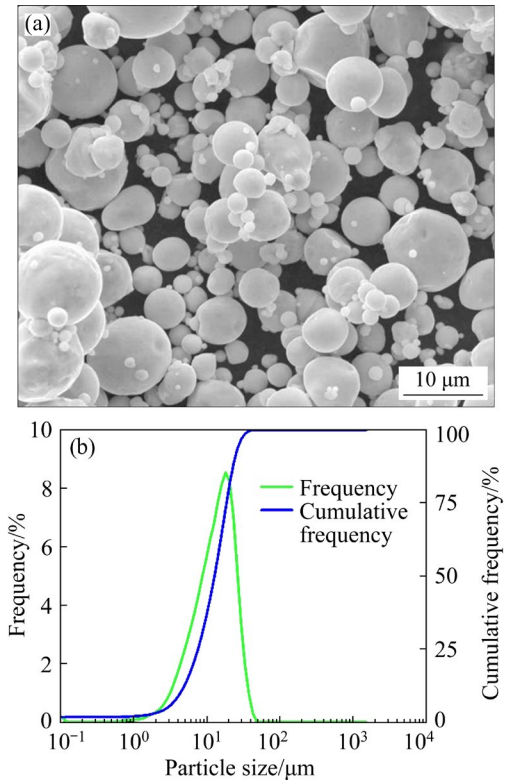

Fig. 1 SEM image (a) and particle size distribution (b) of copper powder

premix solution. Then, the copper powder was added into the premix solution. Next, 2 wt.% (with respect to the mass of the copper powder) of dispersant ZN-1344 was added to avoid pure copper sedimentation and agglomeration. The mixed slurry was then placed in the mixer and stirred continuously for 30 min. Subsequently, 2 wt.% (with respect to the mass of the premixed photosensitive resin solution) of photo initiator TPO was added to the mixed slurry. Finally, the mixed slurry was placed in the planetary ball mill for 2 h to obtain the homogeneous and photopolymerized copper slurry. The composition of copper slurry with different volume fractions of copper are shown in Table 1.

2.3 Printing of green body

The three-dimensional models were created by Creo software, and then Magics software was used to slice the models and generate the supporting structure. Next, the slice data was imported into the self-assembled SLA, operating top-down orientation and a zigzag scanning strategy, which was armed with a high-resolution ultraviolet laser emitting at a wavelength of 355 nm, with the capability of achieving a resolution of 20 μm. The temperature was remained at 26−28 °C and the humidity level at 42%−43%. The copper green body was fabricated by SLA using previously prepared copper slurry. The parameters of the SLA printer were as follows: the layer thickness was 20 μm, the scanning speed was 3000 mm/s, and the laser power was 1055 mW.

Table 1 Compositions of copper slurries of different experiment groups

Group	Volume fraction/%			
	Copper	Monomer	Photo initiator	Dispersant
1	40	55.60	0.84	3.56
2	45	50.24	0.75	4.01
3	50	44.88	0.67	4.45
4	55	39.51	0.60	4.89

2.4 Thermal analysis and post-processing

A proper debinding process and atmosphere can avoid defects in the copper green body and ensure that the organics are thoroughly removed. The mass-loss behavior and calorific change of the green body during de-binding from room temperature to 700 °C were tested with a simultaneous thermal analyzer (STA−449C, NETZSCH, made in Germany) at a heating rate of 10 °C/min under an air atmosphere and a nitrogen atmosphere, respectively. Based on the thermal analysis results, the final debinding and sintering schedule was developed. The process was carried out in a high-temperature atmosphere tube furnace (KJ-T1600-L6010LB1, Zhengzhou Kejia Electric Furnace Company, China).

2.5 Characterization

The viscosity of pure copper slurries was tested with a rheometer (AR2000EX, TA, AR1000, USA) at shear rates of 0.1−1000 s^{-1}. A micrometer caliper was used to measure the curing depth of pure copper slurry and the linear shrinkage of samples with different volume fractions of copper before and after sintering. The density of the sintered copper sample was measured according to the Archimedes theory on a balance with an accuracy of 0.1 mg to guarantee data precision. Hardness measurements were performed with a Vickers hardness tester (HV−10Z, Shanghai Precision Instruments Co., Ltd., China), using a

load and dwell time of 0.5 kg and 10 s, respectively. The microstructure of the cross-section of the green bodies and brown bodies was observed with a field emission scanning electron microscope (FE-SEM, Sirion−200, FEI, America). Brown bodies refer to green bodies that have undergone a debinding process. The surface morphology of sintered parts was observed by a metallographic microscope (OM, Nikon ECLIPSE LV150). Energy dispersive spectrometer (EDS) was used to analyze the chemical composition of brown bodies. In addition, the microstructures of sintered bodies with different volume fractions of copper were characterized. The electrical conductivity of pure copper was tested using a digital portable eddy current conductivity meter (FD−102, First, China) with a calibration specimen of pure copper at 101.3%(IACS).

3 Results and discussion

3.1 Optimization of photopolymerized copper slurry

Slurry for photopolymerization should have a viscosity of less than 3 Pa·s and a solid volume fraction exceeding 40% [28]. Similarly, copper slurry should exhibit low viscosity and sufficient stability to ensure the SLA forming process. Higher solid volume fraction is conducive to improving the relative density, mechanical properties, and physical properties of the sintered parts. Moreover, it can reduce the dimensional shrinkage of the sintered parts. However, viscosity rises as the solid volume fraction increases. Therefore, it is necessary to guarantee that the copper slurry has low viscosity while increasing its solid volume fraction by regulating the type and content of dispersant. Meanwhile, the copper slurry has to be sufficiently stable to ensure that no serious settling occurs during the SLA process.

Figure 2(a) shows the viscosity versus shear rate diagrams of copper slurry using different types of dispersants. The copper slurry added with ZN-1344 had the lowest viscosity of 1.58 Pa·s at a shear rate of 100 s^{-1} compared to other dispersants such as P-5309, which was in full compliance with the viscosity requirement mentioned above. In the meantime, as shown in Fig. 2(b), the relative height of the copper slurry with the addition of ZN-1344 was 86% in 36 h, fully satisfying the stability requirements. For these reasons, the ZN-1344 was

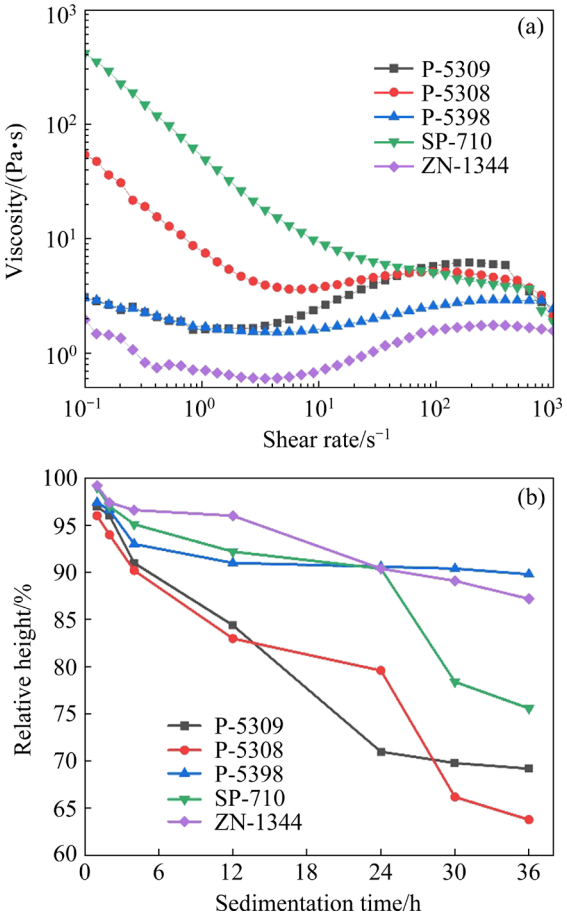

Fig. 2 Viscosity versus shear rate for different kinds of dispersants (a) and relative height of copper slurry for different kinds of dispersants as function of sedimentation time (b)

selected as the dispersant of copper slurry in this work. Additionally, it can be seen from Fig. 2(a) that the slurries showed a transition from shear-thinning to shear-thickening behavior. This phenomenon arises because the fluid inertia force increases, disrupting the laminar flow in slurries at higher shear rates, exacerbating Brownian motion, and leading to shear-thickening [29]. The effect of different ZN-1344 contents on the dispersion characteristics of the slurry system was investigated. From Fig. 3(a), it is evident that copper slurry containing 1 wt.% ZN-1344 exhibited the lowest viscosity at a shear rate of 100 s^{-1}, and the effect of dispersant content on viscosity demonstrated an initial increase followed by a decrease. The reason for this phenomenon is that when the dispersant content is low, long organic chains partially attach to the particle surfaces, resulting in less noticeable steric repulsion effects. As the content increases, the particle surfaces become fully covered with long

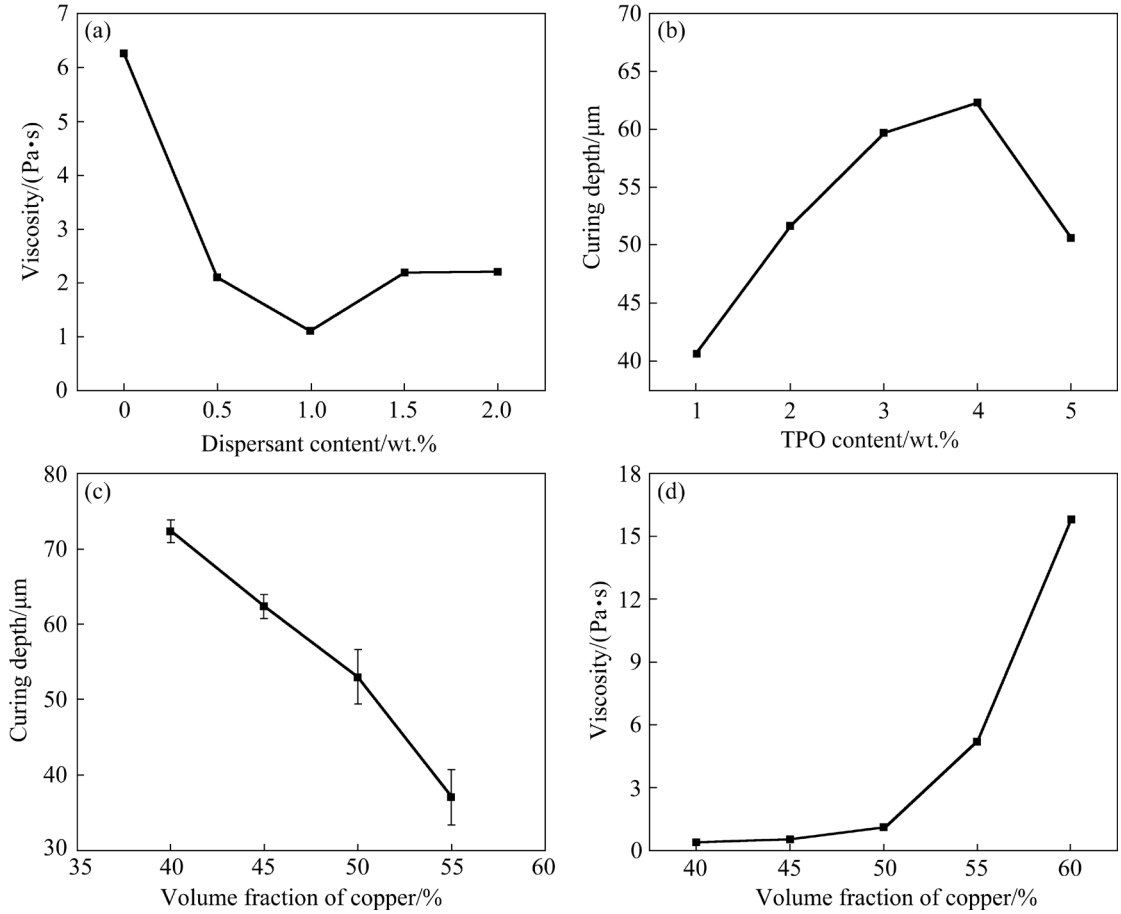

Fig. 3 Effect of slurry viscosity on dispersant content (a), curing depth of copper slurry as function of TPO content (b) and volume fraction of copper (c), and effect of slurry viscosity on volume fraction of copper (d)

organic chains, and the viscosity is the lowest at this time. Nevertheless, if the dispersant content continues to increase, excessive long chains begin to flocculate within the slurry, thereby increasing the viscosity [10].

Figure 3(b) illustrates the effect of TPO content on the curing depth of copper slurry. As the TPO content rises, the curing depth has a tendency to initially grow and subsequently drop, reaching a peak of 62.3 μm at 4 wt.% TPO. This phenomenon occurs because low photo-initiator content results in insufficient free radical generation, weak polymerization, and low curing depth. However, excessive use of initiators significantly influences the circulation of free radicals. Furthermore, an overabundance of photo initiators can lead to further absorption of incident light, thereby diminishing light transmission and consequently reducing curing depth.

Subsequently, slurries with different volume fractions of copper were configured and used for rheological tests and curing depth tests. Figure 3(c) shows the curing depth (C_d) of the copper slurries as a function of volume fraction of copper ($\varnothing$). The C_d values of the copper slurries with volume fractions of 40%, 45%, 50%, and 55% were 74, 58, 45, and 32 μm, respectively. The single-layer printing thickness of the stereolithography equipment was set to be 20 μm, so copper slurries of all groups met the requirements. In addition, the C_d of copper slurries decreased as volume fraction of copper increased, which is consistent with the Beer−Lambert formula [25]:

$$C_d = \frac{2\langle d\rangle n_0^2}{3\tilde{Q}\varnothing\left(n_{Cu}-n_0\right)^2}\ln\left(\frac{E_c}{E_0}\right) \quad (1)$$

where $\langle d\rangle$ is the median particle size of the powder, which is equal to 14.4 μm; n_0 and n_{Cu} are the refractive indices of UV resins and copper powder, respectively; E_0 and E_c are the critical and current UV energy density (mJ/cm^2), respectively; $\tilde{Q}$ is the scattering efficiency term. The principle is that an increase in the solid volume fraction of the copper slurry causes the incident UV light to be

absorbed and reflected. Therefore, copper slurries with different solid volume fractions receive unequal energies at the same depth, and only when the energy at this depth exceeds E_0 can the copper slurry be cured.

Figure 3(d) shows the viscosity of copper slurries with volume fractions of copper being 40%, 45%, 50%, and 55%, respectively. Higher copper volume fraction results in higher viscosity. Moreover, viscosity exhibits an exponential increase when the volume fraction of copper exceeds 50%. The correlation between volume fraction of copper and viscosity can be explained by the function of volume fraction and the relative viscosity in the Krieger–Dougherty equation [30]:

$$\eta_r = \frac{\eta(\varnothing)}{\eta_0} = \left(1 - \frac{\varnothing}{\varnothing_0}\right)^{-n} \quad (2)$$

where η_r is the relative viscosity of the slurry, η_0 is the viscosity coefficient of the medium, $\varnothing_0$ is the limit of the Krieger model, and n is the empirical constant. These values of parameters except copper volume fraction are constant in this work. This phenomenon suggests that the copper volume fraction of slurry plays an essential role in viscosity. The mechanism is that higher copper volume fraction in the slurry increases the number of particles, requiring more liquid to wet them, thereby reducing the free-flowing liquid. Additionally, as the content of copper powder increases, particle spacing contracts. The overlap of the long chains attached to their surfaces increases friction between the particles. Thus, the amount of free-flowing liquid diminishes significantly at sufficiently high solid contents, resulting in considerable particle friction and a dramatic increase in viscosity.

Based on the above results and Ref. [28], the solid volume fraction of copper slurry should not exceed 55% from the perspective of the printing process.

3.2 Debinding and sintering behavior

Organics remaining in the brown body after debinding have a significant impact on the subsequent sintering and the properties of the sample. In order to completely remove the organics, it is necessary to choose the appropriate debinding atmosphere and process. Figure 4 displays the thermogravimetric−differential scanning calorimetry (TG−DSC) curves of TMPTA and HDDA in air and argon atmospheres. Figures 4(a, b) show that in the air atmosphere, TMPTA and HDDA were completely removed prior to reaching 600 °C. Figures 4(c, d) demonstrate that under the argon atmosphere, TMPTA and HDDA were heated up to 700 °C and still had residues. The brown bodies

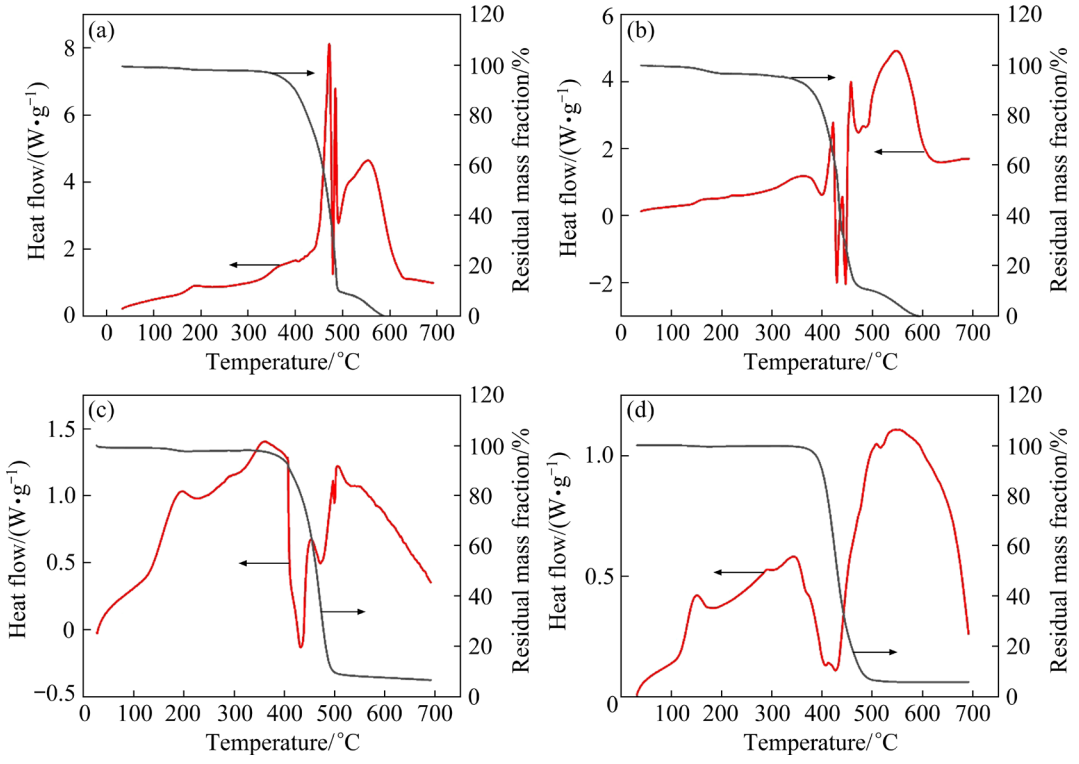

Fig. 4 TG−DSC curves of TMPTA (a, c) and HDDA (b, d) in air (a, b) and argon (c, d) atmospheres

were observed and characterized by SEM and EDS. As shown in Figs. 5(a−c), when the green body was debonded in the air atmosphere, sintering necks clearly formed between the powders, indicating faster sintering behavior compared to the green bodies debonded in nitrogen and hydrogen. Figure 5(d) showed that no carbon was present in the brown body debonded in the air atmosphere, indicating that the organics were excluded completely. This is because, with green body debinding in air, the decomposition of organics is intense and complete, facilitating the formation of contact sites between powders. This is consistent with the above TG−DSC analysis results.

Hence, in order to avoid organic residues affecting the subsequent sintering and the properties of the sample, the pure copper green bodies were debonded in air. But the green body is easily cracked when debonding in air. In this work, the strength of the green body was improved by using copper slurry with high solid volume fraction and adjusting the thickness of the model slices. Consequently, there were no cracks or other defects in the brown bodies. Figure 6 exhibits the (TG−DSC) curves for pure copper green bodies in argon atmosphere. There were three exothermic peaks in the curve, which were 392, 484, and 563 °C, indicating violent decomposition of organics at these temperatures. Simultaneously, the thermogravimetric curve demonstrated a rapid mass loss. When the temperature exceeded 600 °C, the thermogravimetric curve was smooth and unaltered, suggesting that the decomposition of organics was complete, which was in agreement with the results of Figs. 4 and 5. Based on the aforementioned analysis, a rational debinding process including heating rate and holding time was developed, as illustrated in Fig. 7(a).

However, as seen in Figs. 5(a, d), pure copper green bodies were oxidized to copper oxide after debinding in the air atmosphere. Hence, a two-step post-treatment route has to be carried out: debinding and oxidizing of copper green bodies occur in oxidation atmosphere, and then the oxidized copper compound is reduced into highly reactive copper particles under a hydrogen atmosphere, which increases the powder sintering power and enhancing the relative density of samples [31].

Agglomeration of copper slurry inevitably exists, resulting in inhomogeneous components in the green body. In addition, compared with the traditional powder metallurgy process, the green body contains a certain amount of organics and has a lower relative density, which leads to a significant reduction in its sintering capability. Therefore, it is

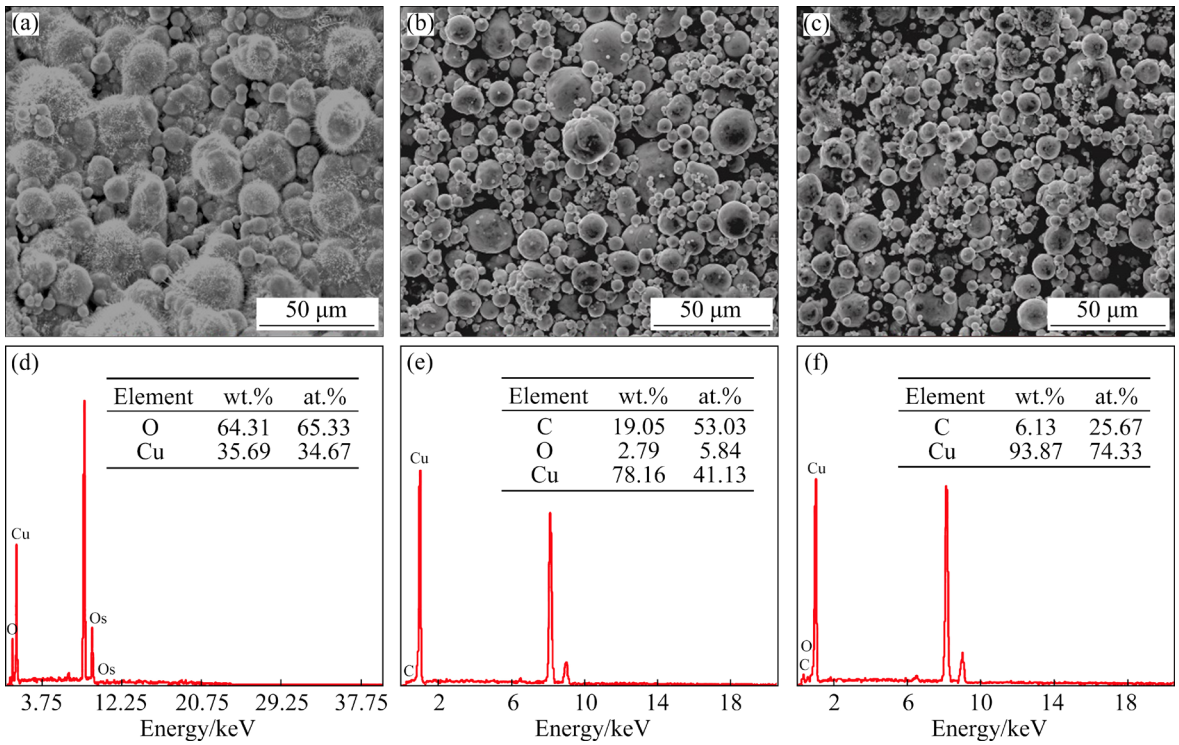

Fig. 5 SEM images (a−c) and EDS data (d−f) of brown bodies in different atmospheres: (a, d) Air; (b, e) H_2; (c, f) N_2

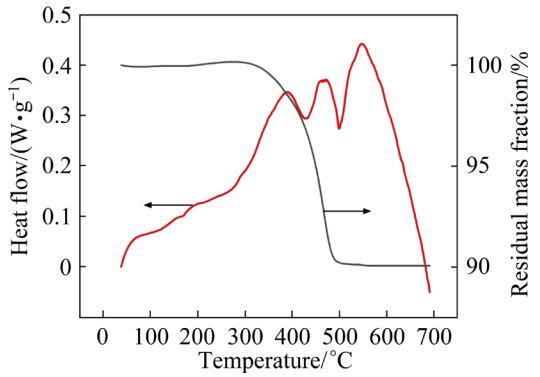

Fig. 6 TG−DSG curves of pure copper green body in argon atmosphere

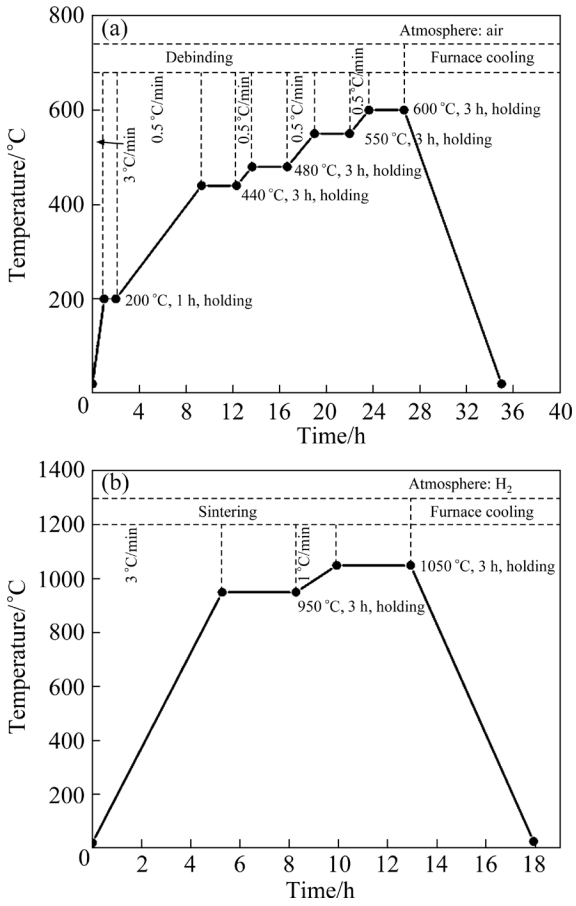

Fig. 7 Debinding curve of pure copper green bodies in air (a) and sintering curve of pure copper green bodies in hydrogen atmosphere (b)

essential to improve and innovate the traditional pure copper sintering process to realize the densification of the samples fabricated by SLA [32]. As a result, the maximum sintering temperature of the current sintering process is 1050 °C, nearing the melting point of pure copper, thereby enhancing the powder sintering activity. In addition, due to the above characteristics of green bodies, the asynchronous sintering phenomenon that the surface layer of the green body is preferentially dense but the interior is loose and porous tends to occur during the sintering process of the brown body [33]. Therefore, in this work, asynchronous densification was attenuated by regulating both the heating rate and the holding time. The sintering procedure is shown in Fig. 7(b).

3.3 Linear sintering shrinkage rate and relative density

The dimensional changes of green bodies with different volume fractions of copper were measured after debinding and sintering. After debinding, the parts were internally porous with insignificant dimensional changes. However, with the brown body sintering, necking between particles occurred and grain boundaries were generated. As a result, the dimensions contracted drastically. Figure 8 shows the relative density and shrinkage of green body after sintering with various copper volume fractions. As can be seen from the figure, the highest relative density (95.4%) and the lowest vertical (19.3%) and horizontal (14.6%) linear shrinkages were found in the group with a volume fraction of 55 vol.%. The higher the copper volume fraction, the smaller the shrinkage. Therefore, it is necessary to compensate for different shrinkages caused by varying solid volume fraction in CAD model design to increase the dimensional accuracy of the part.

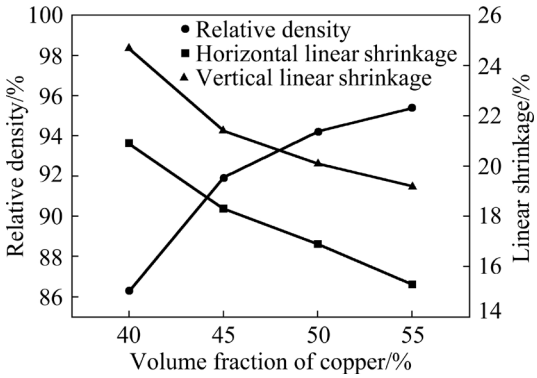

Fig. 8 Variation of relative density and linear shrinkage of green bodies with volume fraction of copper

3.4 Microstructure

Figure 9 shows the optical micrographs of the surfaces of the green bodies prepared with various volume fractions of copper. As observed in Fig. 9, the surfaces of the green bodies exhibited a flat

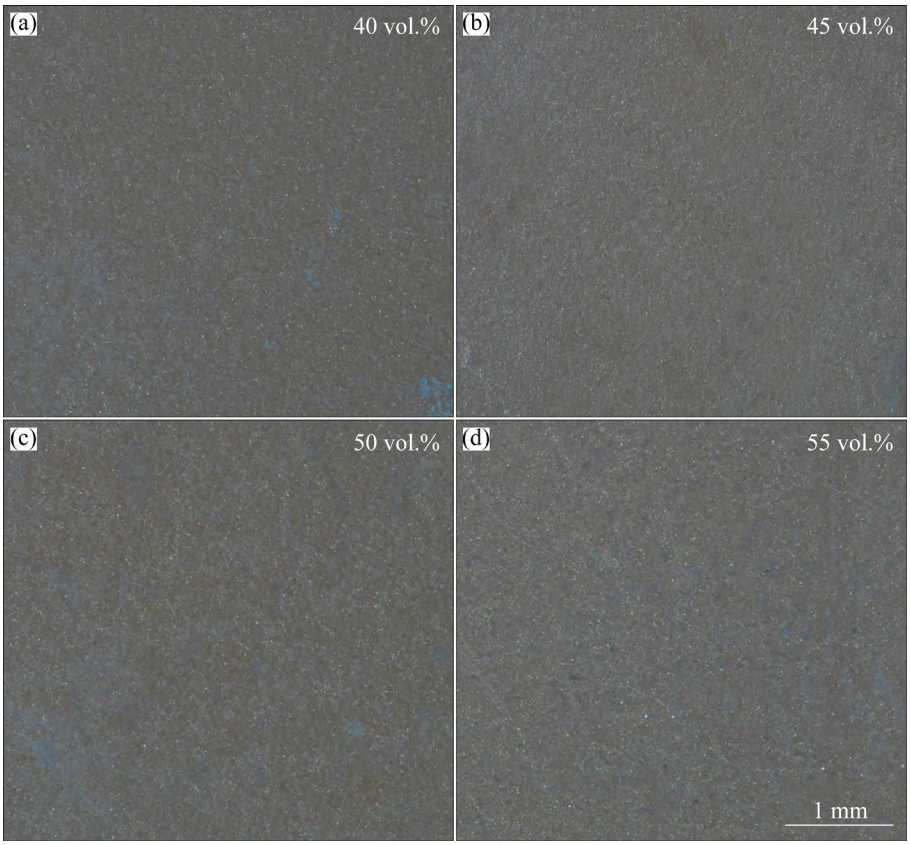

Fig. 9 Optical micrographs of surfaces of green bodies prepared with different volume fractions of copper

appearance without noticeable defects such as holes or cracks, indicating a tight connection between the copper powders bonded by organics. As the volume fraction of copper increased, fewer organic monomers were present on the surface, resulting in a denser particle arrangement. The interlayer bonding significantly influences the subsequent debinding and sintering process. If the interlayer bonding is sufficiently strong, the debinding process is less prone to cracking, warping, and other defects, and the powder particles are more densely packed, promoting subsequent densification. Figure 10 displays the SEM images of the *Z*-direction cross section of the green bodies for all groups. With the increase in copper volume fraction, the curing ability of the copper slurries was attenuated. At the same time, the laminated striation between the layers became increasingly visible. But generally speaking, the layer combination within each group was compact, with no cracking or defects observed, resulting in satisfactory green body quality.

The surface morphologies of the sintered parts are shown in Fig. 11. It is observed that as the copper volume fraction increases, the surface porosity of the sintered part gradually becomes smaller, and at a copper volume fraction of 55%, the surface porosity is virtually eliminated. Samples with higher copper volume fraction demonstrate a tighter powder stack, which facilitates the formation of sintering necks and accelerates sintering process, thereby resulting in fewer pores. This finding aligns with the previously mentioned results of the relative densities.

3.5 Mechanical and electrical properties

The Vickers hardness of SLA-processed pure copper with various copper volume fractions is depicted in Fig. 12. It can be viewed that the hardness of the samples increased with the increase of copper volume fraction and reached its peak at a copper volume fraction of 55% with a value of HV 52.7. This phenomenon is attributed to the corresponding increase in relative density with volume fraction of copper. Sintered parts with higher relative densities indicate improved atomic bonding [34]. Published research [35,36] indicates that pure copper prepared via powder metallurgy

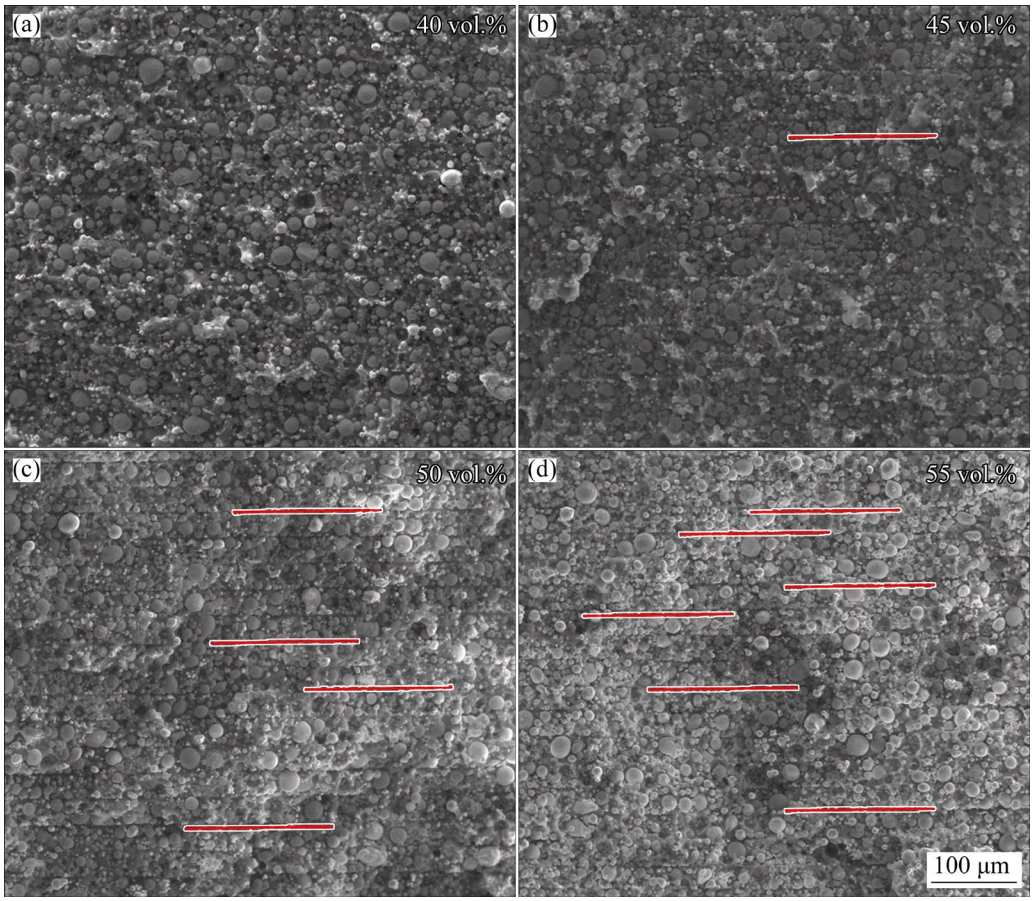

Fig. 10 Cross-sectional SEM images for different copper volume fractions of green bodies (The red lines show laminated striation between layers)

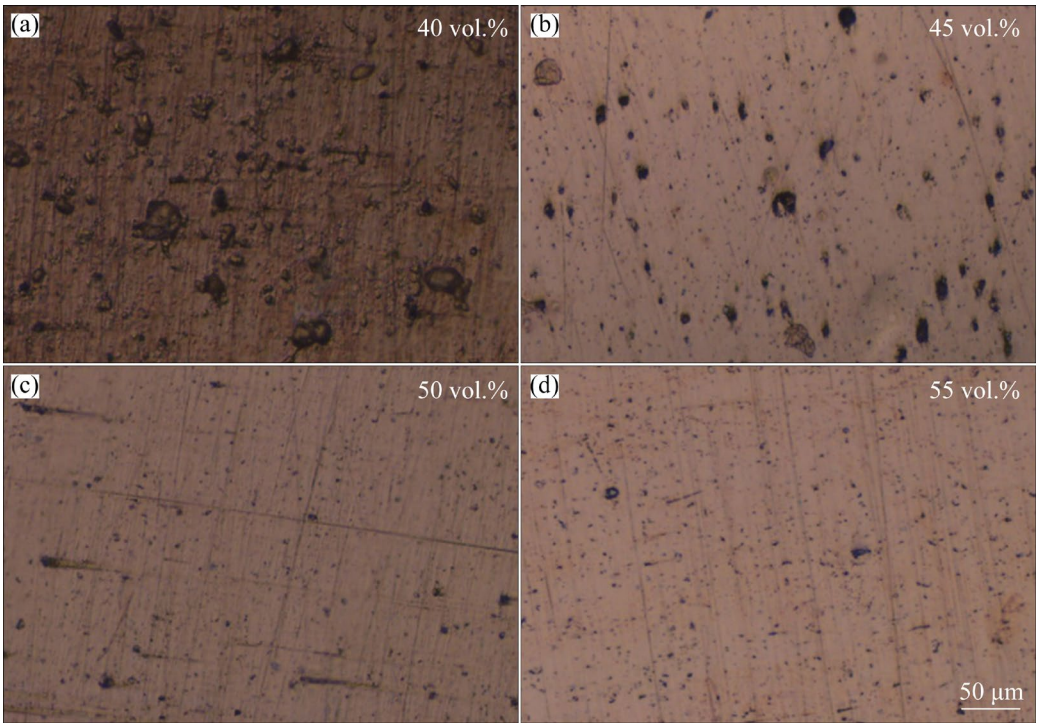

Fig. 11 Surface morphologies of sintered specimens prepared with different volume fractions of copper

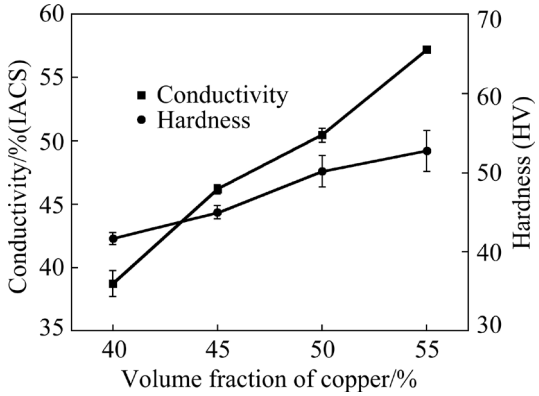

Fig. 12 Conductivity and hardness of sintered specimens prepared with different volume fractions of copper

can achieve a hardness of HV 63. However, the Vickers hardness of the sintered part possessing a relative density of 95.4% in this study is merely 83.65% of this value. It is understandable that the coarsened grains resulting from higher sintering temperature will provide a less hard product than what can be achieved by conventional PM methods.

Electrical conductivity is typically expressed in S/m or as a percentage of the International Annealed Copper Standard (IACS) (100%(IACS)= 5.8001×10^7 S/m). Figure 12 also illustrates the conductivity of IACS for pure copper parts at different copper volume fractions. 55 vol.% of copper parts had the highest conductivity of 57.1%(IACS) due to the high relative density and fewer internal pores, which makes the electrons less susceptible to scattering as they move in the part. It is worth mentioning that the conductivity of samples surpasses that of pure copper fabricated by L-PBF [21].

In view of the above excellent thermal and electrical conductivities of pure copper, in combination with the advantages of high resolution and high surface quality provided by SLA, pure copper fabricated by SLA can be well applied in the field of electronics and thermal management. This technology can allow for the customization of heat sinks, which helps to facilitate personalized product design, optimize the thermal design of the product, and saving die costs. Additionally, the high surface quality of the multi-porous structure will further enhance the thermal efficiency. Figure 13 shows the complex porous radiator structure and school badge of Central South University fabricated by SLA.

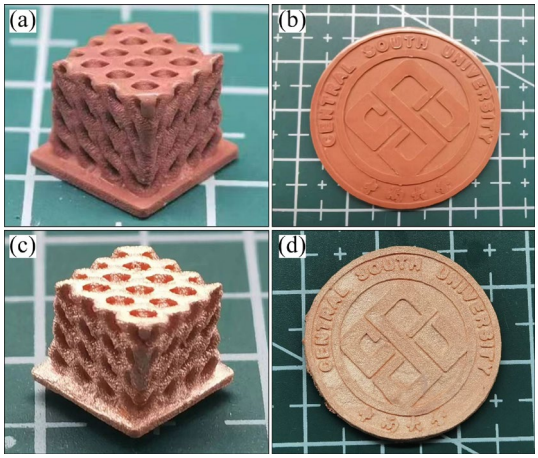

Fig. 13 Green body and finished product of copper samples: (a, c) Complex and porous radiator structure; (b, d) School badge of Central South University

4 Conclusions

(1) The copper slurry with dispersant ZN-1344 exhibited the lowest viscosity of 1.58 Pa·s at a shear rate of 100 s^{-1}. Meanwhile, the relative height of the copper slurry with ZN-1344 was 86% in 36 h, fully satisfying stability requirements for printing.

(2) Slurries with copper volume fractions more than 50% demonstrated a noticeable rise in viscosity, and the maximum volume fraction of copper for SLA processing was 55%. The curing depth of the pure copper slurries decreased with the increase of volume fraction of copper, and the curing depth of the slurries with 55 vol.% copper was 32 μm.

(3) Through the two-step post-treatment method, debinding and oxidizing of copper green bodies occurred in oxidation atmosphere. Then, the oxidized copper compound was reduced into highly reactive copper particles, enhancing the relative density of the samples.

(4) The maximum values of relative density, hardness, and conductivity of samples with 55 vol.% copper were 95.4%, HV 52.7, and 57.1%(IACS), respectively.

CRediT authorship contribution statement

An-liang YE: Validation, Formal analysis, Investigation, Resources, Writing − Original draft, Writing − Review & editing; **Meng WANG:** Validation, Investigation, Writing − Review & editing; **Yan-bin JIANG:** Methodology, Investigation, Supervision, Conceptualization; **Xiao-zan WU:** Validation, Formal

analysis, Writing − Review & editing, Funding acquisition, Resources; **Chao-qun PENG:** Writing − Review; **Jin HE**: Conceptualization, Supervision, Validation, Formal analysis; **Xiao-feng WANG:** Methodology, Conceptualization, Writing − Review & editing, Visualization, Supervision.

Declaration of competing interest

The authors declare that they have no known competing financial interests or personal relationships that could have appeared to influence the work reported in this paper.

Acknowledgments

This work was supported by the Major Science and Technology Projects in Fujian Province, China (No. 2023HZ021005), the State Key Laboratory of Powder Metallurgy, Central South University, China, and Fujian Key Laboratory of Rare-earth Functional Materials, China.

References

[1] SINGER F, DEISENROTH D C, HYMAS D M, OHADI M. Additively manufactured copper components and composite structures for thermal management applications [C]// Proceedings of the 2017 16th IEEE Intersociety Conference on Thermal and Thermomechanical Phenomena in Electronic Systems (ITherm). Orlando, FL, USA: IEEE, 2017: 174−183.

[2] JIANG Yan-bin, LI Yong-shuai, LEI Yu, XIE Jian-xin. Cross-sectional structure, microstructure and mechanical property evolutions of brass cladding pure copper stranded wire composite during drawing [J]. Transactions of Nonferrous Metals Society of China, 2020, 30(7): 1857−1872.

[3] JIANG Yan-bin, LING Liang, XIE Jian-xin. Influences of preparing parameters on surface quality and interface bonding state of brass cladding copper stranded wire by inversion solidification [J]. The Chinese Journal of Nonferrous Metals, 2018, 28(4): 693−704. (in Chinese)

[4] HE Shi-yu, XIONG Ding-bang. Application status of copper-based materials in integrated circuits and prospect on their composites with graphene [J]. The Chinese Journal of Nonferrous Metals, 2023, 33(5): 1349−1377. (in Chinese)

[5] WANG Yang-gang, LI Hao-yang, YUAN Xiao-yan, JIANG Yan-bin, XIAO Zi-an, LI Zhou. Review of copper and copper alloys as immune and antibacterial element [J]. Transactions of Nonferrous Metals Society of China, 2022, 32(10): 3163−3181.

[6] HE Jian-lin, YANG Yang. Quantitative investigation on deformation mechanism and dynamic recrystallization during localized adiabatic shearing of single crystal copper [J]. Materials Science and Engineering A, 2023, 869: 144814.

[7] ZHANG Zhen-feng, LIN Gao-yong, ZHANG Sheng-hua, ZHOU Jia. Effects of Ce on microstructure and mechanical properties of pure copper [J]. Materials Science and Engineering A, 2007, 457(1): 313−318.

[8] WANG Hui-ling, JIANG Feng, TONG Meng-meng, WU Ming-jin, JIANG Jing-yu. Effects of copper-coated MoS_2 on friction performance of bronze-graphite-MoS_2 self-lubricating materials [J]. Journal of Central South University, 2022, 29(11): 3608−3619.

[9] WANG Y H, XIAO L R, ZHAO X J, HU W, SONG Y F, ZHANG W, ZHOU H. Microstructure and mechanical properties of columnar-grained copper produced by the Ohno continuous casting technique [J]. Materials Science and Engineering A, 2015, 639: 122−130.

[10] JIANG Qi, ZHANG Pei-lei, YU Zhi-shui, SHI Hai-chuan, WU Di, YAN Hua, YE Xin, LU Qing-hua, TIAN Ying-tao. A review on additive manufacturing of pure copper [J]. Coatings, 2021, 11(6): 740.

[11] CONSTANTIN L, WU Z, LI N, FAN L S, SILVAIN J F, LU Y F. Laser 3D printing of complex copper structures [J]. Additive Manufacturing, 2020, 35: 101268.

[12] SU Xu-bin, YANG Yong-qiang, YU Peng, SUN Jian-feng. Development of porous medical implant scaffolds via laser additive manufacturing [J]. Transactions of Nonferrous Metals Society of China, 2012, 22(Suppl.): 181−187.

[13] LI Yan-peng, WANG Chang-rui, DU Xiao-dong, TIAN Wei, ZHANG Tao, HU Jun-shan, LI Bo, LI Peng-cheng, LIAO Wen-he. Research status and quality improvement of wire arc additive manufacturing of metals [J]. Transactions of Nonferrous Metals Society of China, 2023, 33(4): 969−996.

[14] YANG Hong, ZHAO Lian-zhong, ZHANG Yan, LUO Hang, WANG Ri-chu, ZHANG Dou, WANG Xiao-feng. Electrical properties of PVDF films fabricated by direct ink writing [J]. Journal of Central South University, 2023, 30(5): 1477−1489.

[15] LYKOV P A, SAFONOV E V, AKHMEDIANOV A M. Selective laser melting of copper [J]. Materials Science Forum, 2016, 843: 284−288.

[16] GUSCHLBAUER R, MOMENI S, OSMANLIC F, KÖRNER C. Process development of 99.95% pure copper processed via selective electron beam melting and its mechanical and physical properties [J]. Materials Characterization, 2018, 143: 163−170.

[17] LEDFORD C, ROCK C, CARRIERE P, FRIGOLA P, GAMZINA D, HORN T. Characteristics and processing of hydrogen-treated copper powders for EB-PBF additive manufacturing [J]. Applied Sciences, 2019, 9(19): 3993.

[18] YE An-liang, JIANG Yan-bin, PENG Chao-qun, WANG Ri-chu, ZENG Jing, WANG Xiao-feng. Research progress on additive manufacturing of copper and its alloys [J]. The Chinese Journal of Nonferrous Metals, 2024, 34(4): 1071−1090. (in Chinese)

[19] ZHANG Jin-liang, SONG Bo, WEI Qing-song, BOURELL D, SHI Yu-sheng. A review of selective laser melting of aluminum alloys: Processing, microstructure, property and developing trends [J]. Journal of Materials Science & Technology, 2019, 35(2): 270−284.

[20] DUTTA B, FROES F H. A the additive manufacturing (AM) of titanium alloys [J]. Metal Powder Report, 2017, 72(2): 96−106.

[21] SILBERNAGEL C, GARGALIS L, ASHCROFT I, HAGUE R, GALEA M, DICKENS P. Electrical resistivity of pure copper processed by medium-powered laser powder bed fusion additive manufacturing for use in electromagnetic applications [J]. Additive Manufacturing, 2019, 29: 100831.
[22] COLOPI M, CAPRIO L, DEMIR A G, PREVITALI B. Selective laser melting of pure Cu with a 1 kW single mode fiber laser [J]. Procedia CIRP, 2018, 74: 59−63.
[23] JADHAV S D, DADBAKHSH S, GOOSSENS L, KRUTH J P, VAN H J, VANMEENSEL K. Influence of selective laser melting process parameters on texture evolution in pure copper [J]. Journal of Materials Processing Technology, 2019, 270: 47−58.
[24] YAO Shu-shan, QIN Xiao-yan, YU Xiao-qiang, ZHANG Qi, XU Guang-hu, WANG Ze-yan, DONG Yi, JING Xiang-yang, SUN Yu-ming, HUANG Bai-biao. Fabrication of grating waveguide using photopolymerization [J]. Transactions of Nonferrous Metals Society of China, 2006, 16(S1): 88−91.
[25] HALLORAN J W. Ceramic stereolithography: Additive manufacturing for ceramics by photopolymerization [J]. Annual Review of Materials Research, 2016, 46: 19−40.
[26] JAVED A, SHAH O, AHMAD S. Optimization of viscosity and composition of mixture of Cu powder and acrylate based resin for vat photopolymerization of metal components [J]. Results in Engineering, 2023, 19: 101307.
[27] LI Yue-meng, LI Chen, ZHANG Xin, WANG Yan-qing, TAN Yong-hao, CHANG Shuai, CHEN Zhe, FU Gang-wen, KOU Zong-kui, STEFAN A, XU Xi, DING Jun. Incorporating metal precursors towards a library of high-resolution metal parts by stereolithography [J]. Applied Materials Today, 2022, 29: 101553.
[28] ZAKERI S, VIPPOLA M, LEVÄNEN E. A comprehensive review of the photopolymerization of ceramic resins used in stereolithography [J]. Additive Manufacturing, 2020, 35: 101177.
[29] BARNES H A. Shear-thickening ("dilatancy") in suspensions of nonaggregating solid particles dispersed in Newtonian liquids [J]. Journal of Rheology, 1989, 33(2): 329−366.
[30] KRIEGER I M, DOUGHERTY T J. A mechanism for non-Newtonian flow in suspensions of rigid spheres [J]. Journal of Rheology, 1959, 3(1): 137−152.
[31] BAI Y, WILLIAMS C B. An exploration of binder jetting of copper [J]. Rapid Prototyping Journal, 2015, 21(2): 177−185.
[32] KRELL A, KLIMKE J. Effects of the homogeneity of particle coordination on solid-state sintering of transparent alumina [J]. Journal of the American Ceramic Society, 2006, 89(6): 1985−1992.
[33] LI He-zhen, SONG Lu, SUN Jia-lin, MA Jing, SHEN Zhi-jian. Asynchronous densification of zirconia ceramics formed by stereolithographic additive manufacturing [J]. Journal of the European Ceramic Society, 2021, 41(8): 4666−4670.
[34] WU Zi-wei, LIU Wei, WU Hai-dong, HUANG Rong-ji, HE Rong-xuan, JIANG Qiang-guo, CHEN Yan, JI Xuan-rong, TIAN Zhuo, WU Shang-hua. Research into the mechanical properties, sintering mechanism and microstructure evolution of Al_2O_3−ZrO_2 composites fabricated by a stereolithography-based 3D printing method [J]. Materials Chemistry and Physics, 2018, 207: 1−10.
[35] MOAZAMI-GOUDARZI M, NEMATI A. Tribological behavior of self lubricating Cu/MoS_2 composites fabricated by powder metallurgy [J]. Transactions of Nonferrous Metals Society of China, 2018, 28(5): 946−956.
[36] GU Ji, NI Song, SONG Min. Effects of torsional deformation on the mechanical properties and microstructures of a commercial pure copper [J]. Journal of Materials Engineering and Performance, 2019, 28(1): 543−548.

基于浆料的光固化增材制造纯铜

叶安梁[1]，王 檬[1]，姜雁斌[1]，伍晓赞[1]，彭超群[1]，何 进[2]，王小锋[1,3]

1. 中南大学 材料科学与工程学院，长沙 410083；
2. 中国科学院 上海光学精密机械研究所 高功率激光器材料重点实验室，上海 201800；
3. 中南大学 粉末冶金国家重点实验室，长沙 410083

摘 要：采用立体光刻(SLA)并结合“氧化−还原”两步后处理法制造复杂形状的纯铜部件。制备了 SLA 用铜浆，并重点考察了铜体积分数对铜浆性能的影响。在两步后处理过程中，通过氧化将生坯内的有机物排除并同时氧化铜粉，再将氧化铜还原成高活性的铜颗粒，进而增加铜生坯的烧结活性，并提高烧结体的相对密度。结果表明：铜浆的固化深度随铜体积分数的增加而减小。当铜的体积分数超过 50%时，纯铜浆的黏度呈指数上升。适用于 SLA 纯铜浆料的最高体积分数为 55%。随着铜体积分数的增加，样品的硬度和电导率增加。当铜体积分数为 55%时，样品的硬度和电导率均达到最大值，分别为 HV 52.7 和 57.1%(IACS)。

关键词：纯铜；增材制造；立体光刻；结构复杂件；铜浆

(Edited by Wei-ping CHEN)